Prompt gamma imaging of proton pencil beams at clinical dose rate

I Perali[1,2], A Celani[3], L Bombelli[3], C Fiorini[1,2], F Camera[2,4], E Clementel[5], S Henrotin[6], G Janssens[6], D Prieels[6], F Roellinghoff[6,7,8], J Smeets[6], F Stichelbaut[6] and F Vander Stappen[6]

[1] Politecnico di Milano, Dipartimento di Elettronica, Informazione e Bioingegneria, Milano, Italy

[2] Istituto Nazionale di Fisica Nucleare, Sezione di Milano, Milano, Italy

[3] XGLab, 20133 Milano, Italy

[4] Università degli studi di Milano, Dipartimento di Fisica, Milano, Italy

[5] iMagX Project, ICTEAM Institute, Université Catholique de Louvain, Louvain-la-Neuve, Belgium

[6] Ion Beam Applications SA, Louvain-la-Neuve, Belgium

[7] IPNL, Université Lyon 1 and CNRS/IN2P3, Villeurbanne, France

[8] CREATIS, INSA, Université Lyon 1, CNRS and INSERM, Villeurbanne, France

E-mail: irene.perali@polimi.it

Received 16 May 2014, revised 30 July 2014
Accepted for publication 15 August 2014
Published 10 September 2014

1. Introduction

1.1. In vivo range control in proton therapy

Proton therapy is a form of radiation therapy that uses high-energy proton beam for cancer treatment. Differently from conventional radiation therapy, proton beams deliver their maximum energy within a defined range, thereby reducing adverse effects to adjacent healthy tissues. However, uncertainties in the determination of this range can impact the applied dose distribution. The sources of range uncertainties are inherent to the limitations of computed tomography (CT) acquisitions, used for treatment planning and range calculations (image noise and conversion of Hounsfield units to proton stopping power). Further sources of uncertainty are related to the patient and include anatomical variations, patient positioning and organ motion. A safety margin between 2 mm and 15 mm is usually added to the target volume in proton therapy, to account for these uncertainties (Paganetti 2012).

For this reason, *in vivo* range verification in proton therapy is highly desirable to reduce margins and deliver safer treatments. Different approaches have been investigated and they can be divided into *direct* methods, that measure proton range by direct dose measurement and *indirect* methods that exploit secondary particles emitted within the patient during proton irradiation. A comparison of the techniques used for *in vivo* proton range verification is summarized in a recent review article (Knopf and Lomax 2013) and the conclusion was that nowadays *in vivo* range control in proton therapy is feasible but a major effort is needed to introduce it into clinical practice. Among *direct* methods, the use of implanted markers (Gottschalk *et al* 2011) and proton radiography and tomography (Schneider and Pedroni 1995, Schneider *et al* 2012) have been investigated on phantoms although results have to be confirmed in clinical studies. The two main *indirect* methods are positron emission tomography (PET) and prompt gamma imaging (PGI). PET imaging makes use of coincident gammas resulting from the annihilation of emitted positrons with electrons. Positron emitting radionuclides, including ^{11}C, ^{13}N and ^{15}O, are generated after nuclear interaction of protons traversing tissue. Detection of positron emission has found growing interest with several active research groups (Enghardt *et al* 2004, Parodi *et al* 2008, Nishio *et al* 2010, Bauer *et al* 2013). PET range verification was already performed successfully with patients (Parodi *et al* 2007) with an accuracy of 1–2 mm for tumours located in low-perfused boney sites. This technique can be used for post-treatment quality control, but it does not offer real-time monitoring. Biological wash-out and organ motion are affecting this excellent accuracy for other sites (Mizuno *et al* 2003, Tomitani *et al* 2003, Knopf *et al* 2009, Helmbrecht *et al* 2013, Hirano *et al* 2013).

PGI uses the prompt gammas emitted by target nuclei that are left excited after interaction with a proton and return to their ground state. In contrast with the PET method, prompt

gamma rays are emitted almost instantaneously and could allow actual real time range verification (Stichelbaut and Jongen 2003). The feasibility of Bragg peak position verification with an accuracy of 1–2 mm was demonstrated by Min *et al* (2006) and Kim *et al* (2007). However, no technical solutions were available so far for a clinical application, because traditional gamma cameras used in nuclear medicine are not adapted for the detection of high energy gamma rays in a huge neutron background. Collimated cameras and Compton cameras have been investigated for this purpose. Collimated cameras were proposed by several groups (Min *et al* 2006, Testa *et al* 2010, Bom *et al* 2011, Kurosawa *et al* 2012) but, as mentioned above, the collimation approach is challenged by neutron background radiation. Different solutions have been suggested. Array type setups (Min *et al* 2012) have been proposed as well as the use of a knife edge slit collimator placed perpendicularly to the beam direction. This approach has been investigated by means of Monte Carlo simulation (Bom *et al* 2011) and experimentally verified by Smeets *et al* (2012). An efficient option to overcome the challenges of detection could be the additional employment of time of flight (TOF) techniques to separate the prompt gamma component from the background radiation (Testa *et al* 2010). In the case of Compton cameras, their main advantage is that they could give the possibility to perform 2D or 3D imaging. However, it is very difficult to achieve a clinically acceptable count-rate because they are based on coincidence measurements. In the literature, mainly double scattering Compton cameras have been studied (Seo *et al* 2007, Peterson *et al* 2010, Kormoll *et al* 2011, Richard *et al* 2011).

Our approach is to image prompt gamma rays with a slit camera exploiting a slit collimator and a pixelated scintillator. A description of this method is given in the next paragraph.

1.2. Prompt gamma imaging with a slit camera

The challenge of PGI is the development of a system that can measure the proton range with both required accuracy and sufficient statistics. The aim of the work was to design and develop a prompt gamma camera that can measure the range of a therapeutic proton beam with a precision (2σ) of 4 mm for individual spots in pencil beam scanning mode. The gamma camera that we realized exploits the concept of a slit camera presented by Prieels *et al* (2011) and shown in figure 1. This variant of the pinhole camera with a slit opening offers better statistics than pinhole collimation. This concept, supported by Monte Carlo simulations, was already validated using the HICAM camera at 100 MeV and 160 MeV (Smeets *et al* 2012) and at 230 MeV (Perali *et al* 2012) with beam currents 100 times lower than the clinical ones (tens of pA). These studies established the feasibility of proton beam range measurement with millimeter accuracy in a homogeneous polymethyl methacrylate (PMMA) target. Despite the nice results obtained with HICAM, several modifications were considered necessary prior to building a new prototype that would be suitable for clinical use. IBA, Politecnico di Milano and XGLab have been collaborating for the realization of such a prototype.

In this paper, we report on the design, development and test of a prompt gamma camera with a slit collimator. The paper is organized in three parts. In the first part, we illustrate the gamma camera architecture in terms of scintillator material and geometry, photo-detectors, electronic front-end and data acquisition. In the second part we present measured characteristics for a prototype limited to 2 of the foreseen 40 channels (Reduced Field of View). In the last section, we present profile measurements of prompt gammas emitted by a PMMA target irradiated by 100 MeV, 160 MeV and 230 MeV proton beams with a current at a nozzle of several nA, measured with the prototype equipped with 20 channels. Using 20 of the 40 channels of the full-size camera allows to have a full FoV but half statistics. For each profile acquisition we evaluated the camera performance for beam range verification, using as quality parameter the minimum number of protons needed to reach a precision lower than 4 mm.

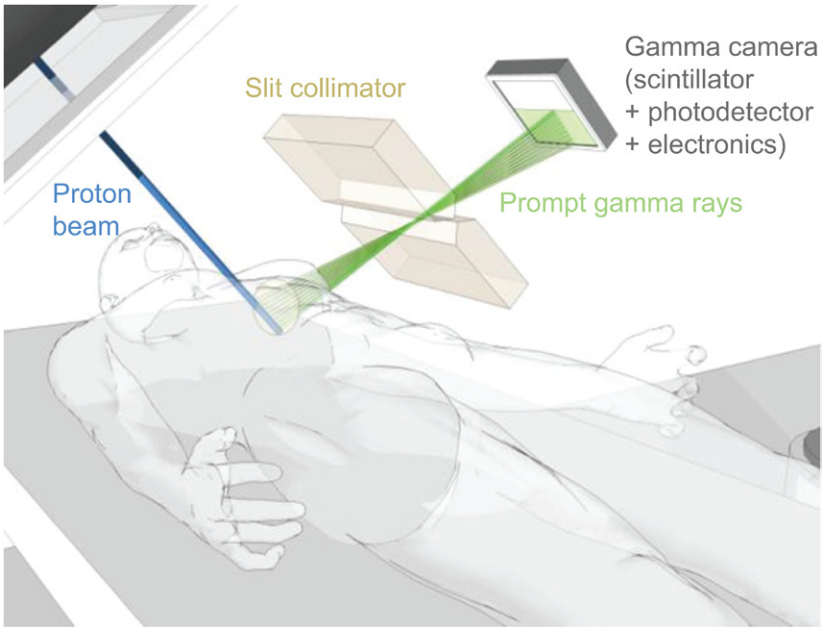

Figure 1. The slit camera concept: a slit collimation gives a 1D projection of prompt gamma emissions along the beam path on a scintillation detector.

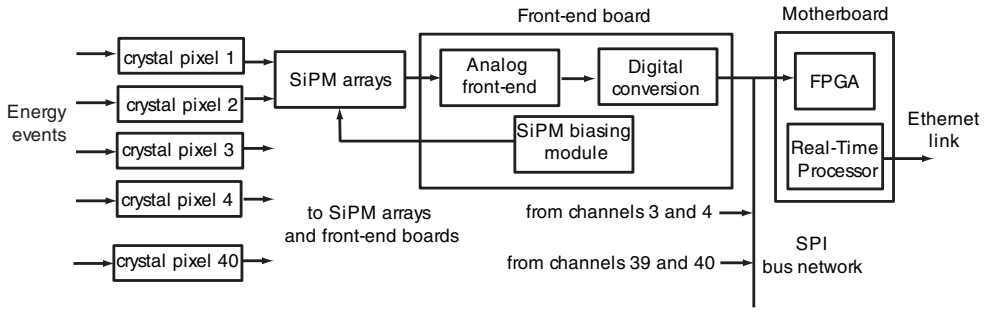

Figure 2. Block scheme of the gamma camera.

2. The gamma camera architecture

The developed system was designed to be clinically applicable. The aim was to produce an instrument that is practical to use, operates at room temperature and uses components compatible with the operation with realistic proton pencil beams.

2.1. Architecture overview

Figure 2 shows the block scheme of the overall design of the developed gamma camera. The system consists of 40 independent channels. The energy-to-visible-light conversion is performed by a scintillation crystal segmented into 40 pixels, directly coupled to 40 Silicon

Photomultiplier (SiPM) arrays. Custom front-end boards perform both the analog readout of the signals coming from the photo-detectors and the digitization of such signals. The data generated after these stages are collected by an acquisition board through Serial Peripheral Interface (SPI) communication. The gamma camera includes also a dedicated power supply unit that provides all the components of the camera (photo-detectors, front-end boards and data-acquisition board) with the required voltage. The gamma camera communicates to the user by means of an Ethernet cable, that allows the remote control of the instrument.

2.2. Scintillator material and geometry

The scintillator material was chosen taking into account the decay time, the light yield and the density.

Short rise and decay times are needed for high count rate measurements; a sufficient light yield is preferred to perform energy selection and high density is required to maximize the photon detection efficiency with respect to the neutron sensitivity. Among high density inorganic scintillators, LYSO ($Lu_{1.8}Y_{0.2}SiO_5$:Ce provided by Saint Gobain) was chosen for its 7.1 g cm^{-3} density, its 32 000 ph MeV^{-1} light yield and, above all, for its short decay time of 41 ns. LYSO suffers from the presence of the beta decaying isotope ^{176}Lu, responsible for a count rate of 276.9 count/s per cm^3 (Saint-Gobain). The upper energy of these counts is the decay energy Q = 1.193 MeV (Ekström and Firestone 1999). They can be eliminated by a hardware threshold and occur at a low rate compared to prompt gamma detections under clinical beam currents.

The crystal volume was dimensioned to leverage several parameters such as counting statistics, spatial resolution and cost. Based on experimental results obtained by Smeets *et al* (2012), we estimated that the minimum crystal volume to obtain 2 mm standard deviation on range estimation is 500 cm^3. In this volume we estimated a count rate of about 10^7 events s^{-1} and a pixelated configuration was chosen to reduce the rate of a single channel: the higher the number of pixels, the lower the rate for a single channel.

The width of the crystal row was fixed to 8 cm in order to have a 10 cm field of view (FOV) on the target, by placing the collimator 25 cm away from the target and the camera 20 cm away from the collimator.

The segment width should be lower than the effective slit width of the collimator. In fact, using the formulation of Anger (1967), for a real slit width of 6 mm, we can compute an effective slit width of 11 mm, which takes into account the penetration of 4.44 MeV photons through the slit knife edges, resulting in a collimator resolution of 22 mm. The same values are obtained using the model of Metzler and Accorsi (2005) for an effective slit width to predict the width of the point-spread-function. The segment width should not be too small because the smaller the width, the lower the probability that the energy lost by a prompt gamma is entirely deposited in a single element. A value of 4 mm was chosen as a good compromise between energy detection efficiency and total number of pixel and so maximum event rate on a single pixel.

A thickness of 30 mm was chosen to reach a satisfying photon detection rate and adapted to the SiPM array size of 31.5 mm to have a 1 : 1 coupling with the photo-detector, maximizing the fill-factor.

Finally, a height of 20 cm was calculated to reach the required volume. To halve the rate on the whole volume, the crystal was divided in two rows of 10 cm height each as shown in figure 3(*a*). The configuration chosen is therefore a crystal made of 40 slabs (20 per row) with a pitch of 4 mm. Each slab has polished surfaces and a reflector only on the opposite face with respect to the output face. Black absorber sheets are placed between the other faces. Each slab

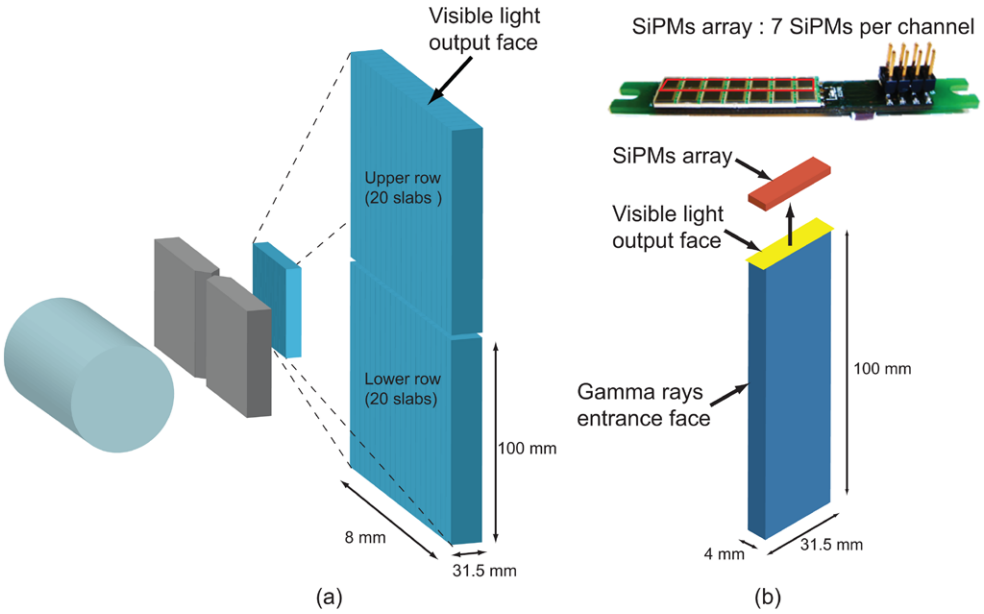

Figure 3. (*a*) System configuration: the system consists of a slit collimator that collimates the gamma rays emitted by the target to produce a 1D projection on a pixelated scintillator. (*b*) Crystal-to-photodetector coupling. The custom SiPMs array (7 SiPMs) is directly coupled to the smallest face of the crystal slab. 2 SiPMs arrays are mounted on the same PCB. Figures are not to scale.

acts as a light-guide and the visible light is collected from the top and bottom faces of the two rows as shown in figure 3(*a*).

2.3. Photo-detector configuration

To take advantage of the pixelated configuration, 1 : 1 coupling of crystals with the photo-detector is needed. The Silicon Photomultipliers were chosen as the best devices to detect the visible light, for their fast response, photon detection efficiency (PDE) of about 0.5, compact size and low cost. For these reasons this kind of photo-detector is nowadays gaining interest for the use in state-of-the-art PET systems.

The model chosen has an active area of 3×3 mm^2 and a number of microcells equal to 3600. The single devices were arranged in arrays of 7 SiPMs each, to fit exactly the crystal light output face as shown in figure 3(*b*). A photograph of the photo-detectors mounted in the 2×7 array configuration is shown on the right on the same figure. The coupling was made with silicon optical grease and without the use of light guides. The fill-factor, defined as the ratio between the active area and the crystal output face area, is 0.5. We evaluated (and then confirmed with measurements) that this loss of light is admissible to reach the requested energy resolution.

2.4. Electronics front-end

Custom electronics boards were designed to read out the signals coming from the SiPM and convert them to digital values. In the gamma camera, 20 identical printed circuit boards (PCB)

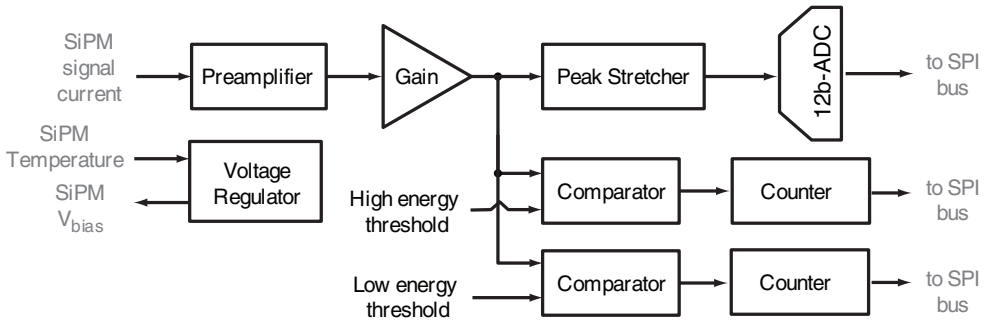

Figure 4. Conceptual schematic of the front-end electronic boards.

are used to read out the signals coming from the 40 SiPMs arrays (each board is used for the simultaneous acquisition of the signals coming from two channels). The choice of the components aimed to reduce as much as possible the cost, while maintaining satisfactory performance.

The conceptual schematic of the board is shown in figure 4. The current-to-voltage conversion is performed by an integrator preamplifier stage. The integration time constant of this stage was chosen to reach a good energy resolution, without widening the pulse shape too much. Short pulses are needed to avoid the pile-up of the very frequent events. The first stage is followed by a gain stage, that amplifies the amplitude of the pulses to exploit totally the voltage dynamic range of the electronics (0–3.3 V). The signal path is then split to manage the pulses in different ways according to the kind of measurement performed. The peculiarity of the design is indeed the possibility to switch between two modes of operation that we will identify as *slow* and *fast*, because they have different count rate capabilities. The *slow* mode section consists of a peak stretcher followed by a low-cost Analog to Digital Converter (ADC, 12 bit, 500 ksps), that performs an analog to digital conversion of the amplitude of each pulse and reconstructs the energy spectra. The spectra collected using this mode of operation are necessary for the energy calibration of the camera. Since one ADC is shared between two channels, the event rate must be kept below 2×10^5 events s^{-1}, which is more than enough for spectra acquisitions with commonly used radiation sources with an activity of 100 kBq.

The *fast* mode is used for the acquisition of prompt gamma profiles. In this modality, the board operates in fast photon counting mode and counts the events between two hardware thresholds, corresponding to two energy levels, set after energy calibration. The comparator and the counters are fast components and they can potentially accept short pulses at a rate of 3×10^7 events s^{-1}. Actually, the limitation in count rate capability is the width of the pulses, that is mainly determined by the decay time constant of the scintillator.

The same PCB includes also a voltage regulator that adjusts the SiPM array biasing voltage according to the temperature, in order to keep the SiPM gain constant.

2.5. Data collection and analysis

As reported in the previous paragraph, the analog to digital conversion is implemented at the front-end board level. A motherboard is needed for the collection of the data coming from the 20 front-end boards. For this purpose, an embedded control and acquisition device from National Instruments was chosen. The selected device integrates a real-time processor, a user-reconfigurable FPGA and Input/Output on a single printed circuit board. The data coming from the front-end boards are downloaded to the motherboard exploiting an SPI protocol in

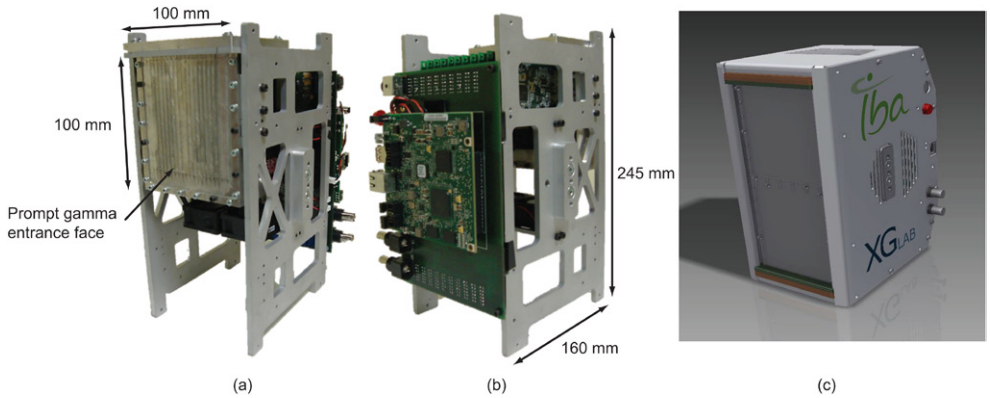

Figure 5. Photographs of the front-view (*a*) and back-view (*b*) of the realized camera consisting in 20 channels. (*c*) Rendering of the full-size camera.

the bus network configuration. The motherboard communicates with a central control unit with an Ethernet cable. All the basic processing operations are performed at the microcontroller level in order to reduce the data flow and so the time to download them to the PC. With this on-line processing, we avoid the handling of huge amount of data, by sending only the valid information. In the case of the spectra acquisition, 4096 values are sent from each channel to the motherboard. In the case of profile acquisition, each channel sends the number of summed counts in the energy range of interest; that means 40 numbers for the whole camera.

2.6. Mechanical structure

Compactness was given high priority to enable close access to the patient during treatment. Figure 5 shows pictures of the camera: for the first experiments only half detector (20 channels, i.e. half crystal volume) was mounted. In the picture on the left the aluminum case that encloses the crystal is visible: it guarantees scintillator-to-photodetector alignment and it shields the SiPMs from visible light. The picture in the middle is the back view of the camera with the motherboard and the back-plane board. The dimensions of the mechanical structure are indicated on both pictures. The picture on the right shows the final appearance of the gamma camera, covered by an aluminum case.

3. Performance evaluation with a 2-channels prototype

3.1. Experimental setup and methods

Before the construction of the full-size camera, a prototype limited to 2 channels was developed and tested in order to benchmark the main choices made during the design phase. The crystal geometry (slab dimensions), the photo-detector configuration, the front-end electronics and the data collection are the same as in the full-size camera. The system is a laboratory-oriented prototype: for this purpose compactness and engineering of the assembly are not required. A sketch of the prototype is shown in figure 6. The 2 crystal slabs are enclosed in an aluminum case with absorber sheets on the lateral surfaces and reflectors on the small surfaces, opposite to the light output face. The crystals are directly coupled to 2 SiPM arrays (7 SiPMs each) with optical grease (Saint-Gobain BC630). SiPMs are mounted on the top-side

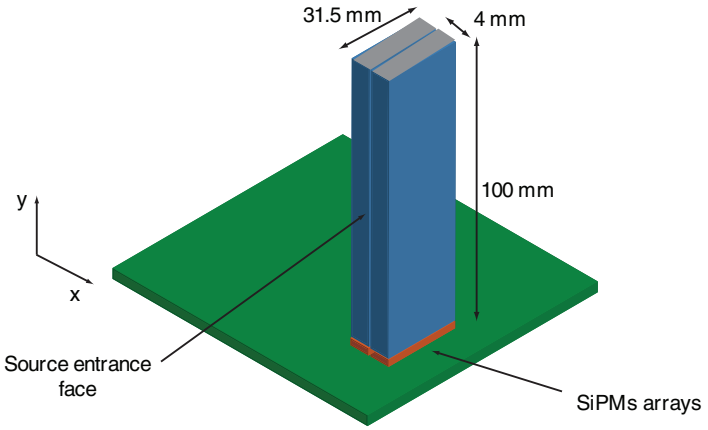

Figure 6. 3D sketch of the 2-channel prototype crystal configuration used for characterization measurements. The crystals slabs are enclosed in an aluminum case and directly coupled to the SiPMs array mounted on the top-side of the front-end PCB.

of the PCB, which includes the front-end electronics. In contrast to the final prototype, all the components (including SiPMs) are biased by external laboratory power supply units.

The first critical point of the design was the geometry of the crystal, that is long and thin. The experiment described in this section was undertaken to verify that the energy detection does not change along the height of the slab.

A ^{137}Cs collimated source was used for this purpose, using a collimator opening of 1mm. The experimental setup is shown in figure 7 and consists of the 2-slabs module and the collimated source placed on an $x - y$ translator. The camera was placed in a fixed position and the collimated source moved along the y direction by steps of 20 mm from the central position (0 mm) at –40 mm, –20 mm, 20 mm and 40 mm. For each position of the source we acquired a spectrum, operating the camera in *slow* mode. For each spectrum, the background due to the LYSO activity was subtracted and the ^{137}Cs photopeak was fitted with a Gaussian distribution.

3.2. Experimental results

In figure 8(*a*) the spectra obtained in the 5 different positions are superimposed. The centroid of the Gaussian distribution was plotted versus the position of the source along the *y*-axis in figure 8(*b*). The maximum relative variation of the peak is 3%.

The conclusion of the experiment was that there is no significant dependence of the detector response on the position of interaction along the height of the slab. The slab configuration is suitable for event discrimination only along the horizontal direction, as needed.

4. Prompt gamma measurements with the prototype

4.1. Materials and methods

4.1.1. Experimental setup. Knowing that the spectra are uniform along the height of the crystal, a second prototype, consisting of a single row of 20 crystal slabs, was mounted and tested at the West German Proton Therapy Centre Essen (WPE). This prototype has half channels with respect to the designed camera and so it has half the volume of the final camera.

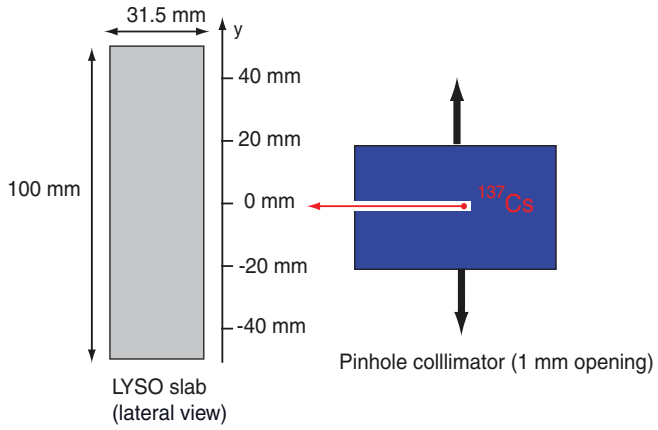

Figure 7. Schematic of the experimental setup used for the position sensitivity characterization on the vertical axis.

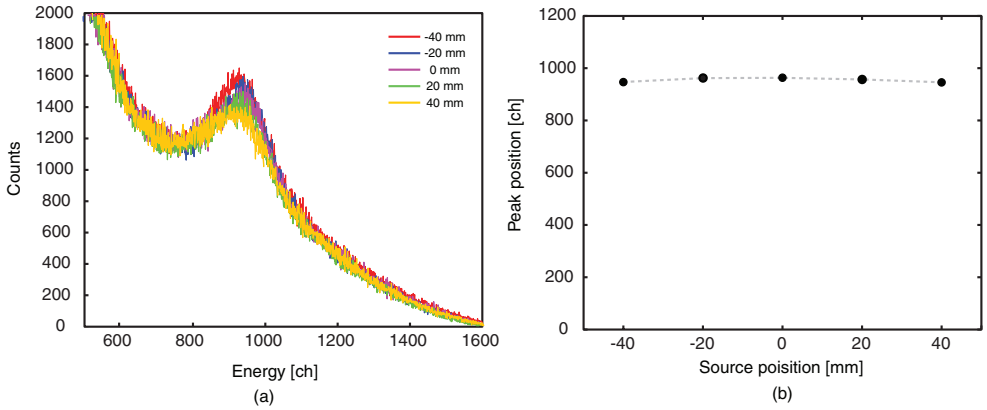

Figure 8. (*a*) Superposition of the spectra collected at different positions of the source along the height of the crystal. (*b*) Energy peak position versus source position along the height of the crystal

Nevertheless, with this configuration we were able to detect prompt gamma profiles with the same FoV as the full-size camera, but with reduced statistics.

The experimental setup is shown in figure 9. Proton pencil beams of 100 MeV, 160 MeV and 230 MeV were delivered along the axis of the cylindrical PMMA target. The target has a radius of 7.5 cm and a length of 20 cm or 40 cm according to the beam energy (20 cm for 100 MeV and 160 MeV, 40 cm for 230 MeV). The tungsten alloy collimator (16.96 g cm^{-3} with 90% W, 6% Ni and 4% Cu) was located 25 cm from the beam axis and 20 cm from the camera. The collimator has 4 cm thickness, 63° slit angle, 6 mm slit width, 12 cm height and 16 cm length along the beam axis for each block. The camera and the collimator were centered at the expected beam range depth at 100 MeV, 160 MeV or 230 MeV. Measurements with a closed collimator were also performed by joining the right-angled faces of the two tungsten blocks, resulting in a tungsten wall. For each acquisition, the number of protons delivered was recorded with a large parallel plate ionization chamber intercepting the beam.

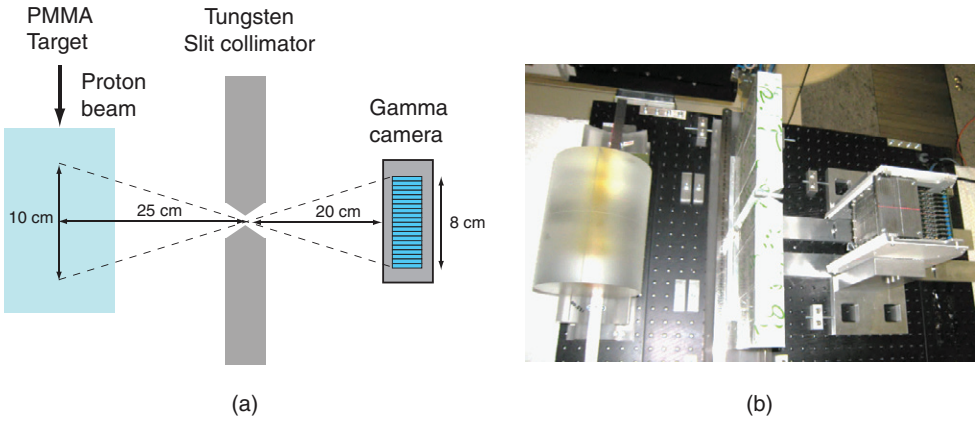

Figure 9. Schematic (*a*) and photograph (*b*) of the experimental setup including the cylindrical PMMA target, the tungsten slit collimator and the camera.

4.1.2. Spectra acquisition and energy calibration. A first order calibration of the camera at low energies had been done in Politecnico di Milano with the use of the ^{137}Cs 662 keV peak and the two peaks of ^{60}Co (1173 keV and 1332 keV). The points were fitted with a linear equation to determine a calibration which is effective at low energies. According to our evaluation, the large amount of light produced by LYSO with energies up to 10 MeV, would lead to the saturation of the SiPMs microcells (Grodzicka *et al* 2011) and the calibration curve would follow the equation:

$$E(\text{ch}) = a(1 - \text{e}^{-bE(\text{keV})}) + c \tag{1}$$

where a, b and c are parameters that take into account the variability among channels. In particular a depends on the overall gain of the SiPM array and on the electronics gain; b is related to the scintillator light yield, the transmission efficiency, the SiPM PDE and the electronics integration time and c results from the sum of all the offset contributions. The coefficients a, b, c can be precisely determined with a calibration that includes high energy points: we use the activity of the PMMA target hit by the proton beam to find out these points. For this purpose, the camera was operated in *slow* mode and the hardware energy threshold set to 400 keV, according to the first order energy calibration. We use a proton beam of 100 MeV with a beam current of 280 pA: this low current value was selected so as not to saturate the electronics rate capability in *slow* mode. For this kind of measurement, the collimator was removed to obtain better statistics. The linear energy calibration was used to define intervals within the ADC dynamic range, where characteristic peaks should be found and helped in the identification of such peaks. The points were fitted using equation (1), which was used to determine the relationship between energy and ADC channels for the setting of the thresholds.

4.1.3. Data treatment for profile acquisitions. After the energy calibration, the camera was switched to *fast* mode of operation and two hardware thresholds were set to discard the events below 3 MeV and above 6 MeV. For each channel, the number of counts above the higher threshold was subtracted from the number of counts above the lower threshold and the profile was reconstructed as the histogram of the summed counts for each crystal slab.
The profiles were not corrected for dead-time. As a first approximation, the system can be modeled as paralyzable, with a dead-time corresponding to the average time over threshold

for each energy event. However, the effect of dead-time is no more than a few percent up to maximum clinical beam current with the C230 accelerator. Further dedicated investigations are needed since this correction is potentially dependent on the whole energy spectrum (and thus on the target composition and the camera configuration).

Most acquisitions were performed for 10 s in order to have excellent statistics for a much higher dose than in practice. This was done to observe the uniformity independent of statistical considerations. The main cause of non-uniformity in the profiles could be caused by the non-perfect independent energy calibration of all channels. A correction by means of a uniformity map was not applied as this would be valid only if the uniformity map and the profile to be corrected have an identical energy spectrum.

For each acquisition we evaluate the performance of the camera by quantifying the minimum number of protons needed to achieve a precision in range retrieval less than 4 mm. We can consider that, in an homogeneous target, a range error results in a shift of the profile with respect to a reference profile, which, in clinical application, would be a simulation. For our experiment as a reference profile we used the high dose 10 s long acquisitions, during which approximately 10^{11} protons are delivered and which can be considered without noise. This reference acquisition was then rescaled for different number of protons and Poisson noise was added to each rescaled profile.

A 20 mm Gaussian smoothing was applied to all profiles. This smoothing, in addition to removing statistical noise, was so far found to be the most practical solution for efficient uniformity correction. With this smoothing, no significant information is lost since the collimator effective geometric resolution is not better than 20 mm, as stated in section 2.2.

The shift retrieval between the reference and the noisy curves was obtained using a root-squared difference minimization. The reference profile was shifted along the camera axis with a step of 0.2 mm along the x-axis. For each shift of the reference profile we calculated the integral of the square root of the difference between the profile and the shifted reference profile. The best match is the one that minimizes this sum and the shift corresponding to this match is the shift between the two profiles. Ideally, in absence of noise, we should retrieve a shift of 0 mm with any deviation corresponding to the error. For each level of dose, the retrieval was performed 1000 times with different occurrences of Poisson noise, to obtain high statistics. We calculated the standard deviation of the error distributions and considered 2σ as estimator for the precision of the system. If we plot the 2σ of the distributions versus the number of protons in a logarithmic scale, the data have a linear trend because the precision is proportional to the inverse of the square root of the number of protons. From this trend we can determine the number of protons needed to reach a defined level of precision. For our evaluation, we considered a precision of 4 mm. The number of protons is always expressed as a multiple of 10^8 protons, which is a realistic order of magnitude for the number of protons delivered in a fraction of a distal spot in clinical practice.

4.1.4. Configurations for profile acquisitions. Profile acquisitions were performed in different configurations of setup, beam properties and acquisition settings in order to evaluate the dependence of the performance of the camera on different parameters. The following acquisitions were performed:

- *Range control*: at beam energies of 100 MeV and 160 MeV (beam currents of 1.85 nA and 5.6 nA, respectively), the target was moved along the beam axis to emulate a range shift at 8 different positions (−1, −2, −3, −5, −7, −10, −15, −20 mm) with respect to the central one (0 mm). For each acquired profile we retrieved the range shift with the method described in section 4.1.3, using the 0 mm profile as a reference. The mean absolute error

of range retrieval was found for different levels of dose by calculating the mean of the absolute values of the errors for 1000 profiles.

- *Acquisitions at different beam energies*: profiles at 100 MeV, 160 MeV and 230 MeV were acquired at beam currents of 1.3 nA, 1.8 nA and 4.6 nA and with the collimator in place. One acquisition with the collimator closed was made to detect the uncorrelated contribution. This acquisition was then subtracted from the acquisition with the collimator open, to isolate the correlated contribution. Profiles were compared to Monte Carlo simulations performed with the code MCNPX version 2.5.0, using the same settings described in the previous work of Smeets *et al* (2012). We first compared the acquisitions obtained in the two collimator configurations and then only the correlated contribution. Simulations were rescaled in order to obtain the best match with the acquired profile according to the root-squared difference minimization between acquisition and simulation.
- *Acquisitions in different energy windows*: the optimal energy range of 3–6 MeV had been determined after the simulation study performed by Smeets *et al* (2012), that applied a decomposition in energy groups of 1 MeV of the photon-simulated detection profile. The authors observed that photons below 1 MeV are not correlated with the range, but higher energies, mainly produced by primary protons along the beam path and not much affected by scattering before leaving the target, have a fluence correlated with the beam range. In particular, the 4–5 MeV photons give the most interesting contribution. To verify the results of this simulation study, we acquired profiles in 9 energy windows from 1 MeV to 10 MeV in steps of 1 MeV. The beam energy was 160 MeV.
- *Measurement of the entrance point*: we investigated the possibility to use an additional slit camera to measure the entrance point in the patient. The idea is to have a slit camera which measures a shift for the expected penetration depth and a second camera which measures a shift for the entrance point, so that a range shift could be interpreted correctly if it resulted from a movement of the patient with respect to his position in the treatment plan. A single slit camera could not reasonably image the whole proton track as range goes up to 32.9 cm in water. For the measurement of the entrance point, the PMMA target was moved to have the lateral face aligned with the collimator aperture.
- *Acquisitions at different beam currents*: we tested the count-rate capability of the camera in very challenging conditions in terms of event rate. For this experiment, we applied a modification to the setup depicted in figure 9. The camera was placed closer to the target (30 cm instead of 45 cm) and the collimator was placed half-way between the camera and the target. We adopted this setup to double the number of events on the scintillator. The energy of the beam was 230 MeV and the beam current was raised to different values up to 28 nA, i.e. 6 times higher than the value used in clinical routine. For each 10 s long acquisiton we found the maximum rate on a single channel by dividing the maximum value of each profile for the acquisition duration.

4.2. Results and discussion

4.2.1. Acquired spectra and calibration curve. Figure 10(*a*) shows the spectrum acquired with a single channel; the 19 spectra collected with the other channels are similar. The photon detection efficiency of the thin LYSO slab is poor, nevertheless weak bumps in the spectra can be interpreted thanks to the list of nuclear de-excitation gamma rays established by Kozlovsky *et al* (2002). Identified peaks are marked in figure 10 and listed in table 1. In the spectrum, single- and double-escape peaks are visible for the 4.44 MeV peak and the double-escape peak is visible for the 6.129 MeV peak. Figure 10(*b*) shows the energy calibration curve obtained

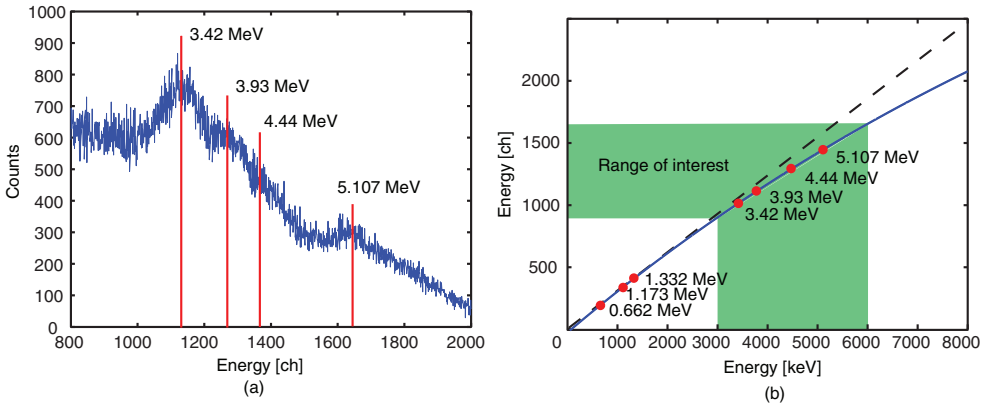

Figure 10. (*a*) Spectrum measured for 100 MeV protons without a collimator. Measured gamma peak energies are marked with a vertical line. The values on the *x*-axis are the ADC channels. (*b*) Energy calibration curve. The linear calibration obtained from ^{137}Cs and ^{60}Co peaks is depicted with a dashed line. The events recorded during the acquisition of the profiles are highlighted in green.

Table 1. Energy and interpretation of the peaks in the spectrum at 100 MeV without collimator (based on Kozlovsky *et al* (2002)).

Peak energy (MeV)	Interpretation
$3.42 = 4.44 - 2 \times 0.511$	^{12}C(p,p*)^{12}C*
$3.93 = 4.44 - 0.511$	^{16}O(p,x)^{12}C*
4.44	^{12}C(p,sp)^{11}B*
$5.107 = 6.129 - 2 \times 0.511$	^{19}O(p,p*)^{16}O*

using the points identified from the spectrum fitted with equation (1). On the same figure, the linear calibration performed with ^{137}Cs (0.662 MeV) and ^{60}Co (1.173 MeV and 1.332 MeV) is shown: the linear and the exponential curves are quite coincident at low energies but they diverge one from another above 3 MeV, confirming that the exponential calibration is necessary in the energy range of interest. The hardware thresholds were set to 3 MeV and 6 MeV, that correspond to about 900 ADC channels and 1600 channels, respectively (for each channel the threshold values were set according to its calibration curve). The energy range of interest for prompt gamma acquisition is shown in green.

4.2.2. Data treatment applied to acquired profiles. Figure 11 shows profiles acquired with the collimator closed (left) and with the collimator open (right) for a 160 MeV proton beam and a beam current of 1.8 nA. On both plots, the raw data, corresponding to the number of summed counts between the energy thresholds normalized to the number of delivered protons (1.14×10^{11}), are depicted in blue. The profile after the Gaussian smoothing is illustrated with a red line. The acquisition with the collimator closed is almost flat along the detector axis, showing that this contribution, mostly constituted of neutrons, is not correlated to the beam range within the target. For the acquisition with the collimator open, the profile shows an evident fall-off in correspondence to the center of the detector (0 mm), that was aligned to the expected beam penetration in the target.

Figure 12 is an example of the profile rescaled for different number of protons (10^7, 10^8, 10^{10} and 10^{12}), with the addition of noise, showing the impact of the noise on the quality of the profiles as a function of the number of protons.

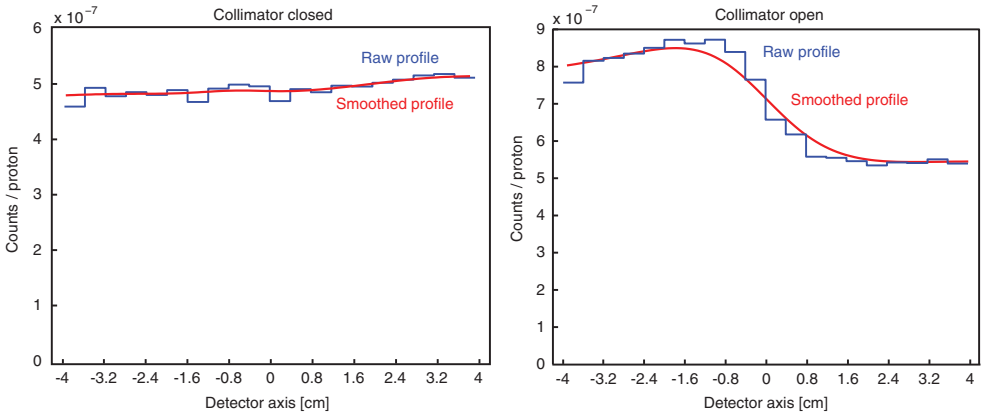

Figure 11. Comparison between a profile before (blue line) and after (red line) smoothing. The profile was acquired with a beam energy of 160 MeV and with the collimator closed (left) and open (right).

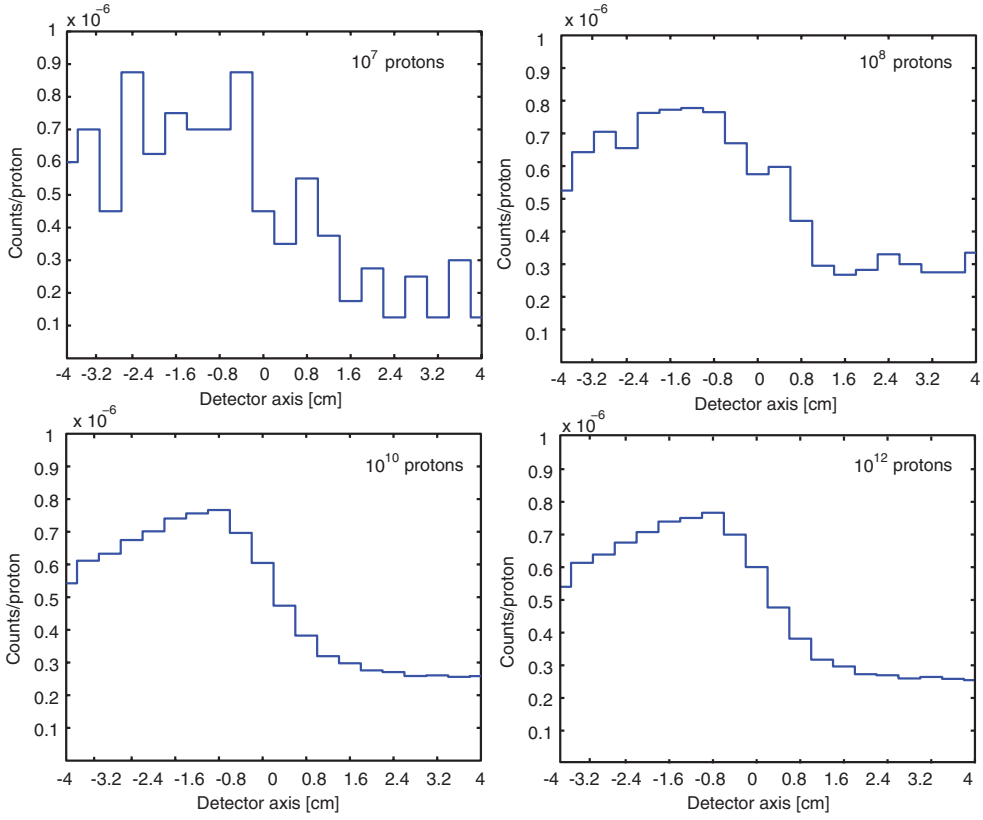

Figure 12. Detection profiles resampled for different number of protons.

As already stated, the effect of statistical noise can result in the detection of a shift of the profile with respect to the reference profile, so that this shift can be considered as the error. The precision (2σ of the error distribution) at different levels of dose is plotted in figure 13. From this

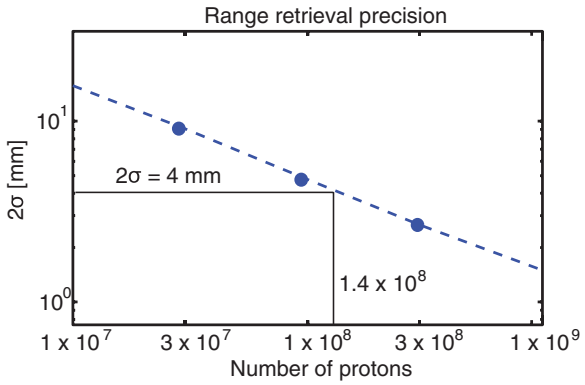

Figure 13. Range retrieval precision (2σ) versus the number of delivered protons. The number of protons needed to reach a precsion of 4 mm is highlighted in the graph.

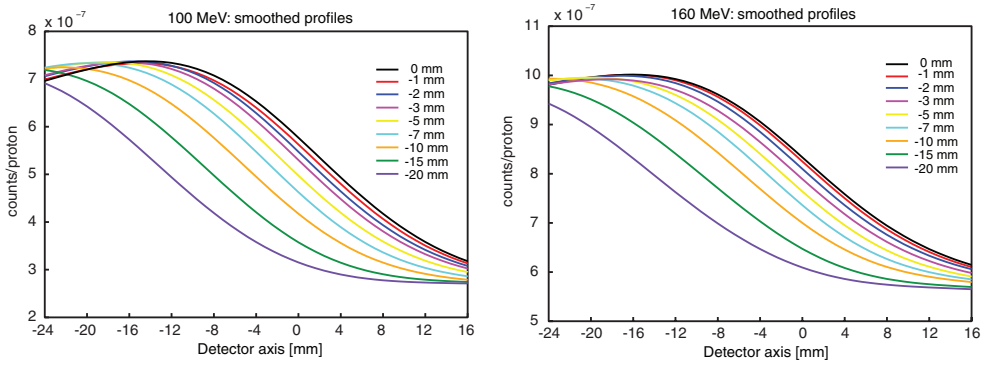

Figure 14. Detection profiles measured at 100 MeV (left) and 160 MeV (right) as the target is moved along beam axis to induce the detection of range shifts by the camera. The acquisitions at 100 MeV and 160 MeV were realized for 1.15×10^{11} and 3.5×10^{11} incident protons, respectively.

log-log plot we can observe a straight line behavior, confirming that the precision is proportional to the inverse of the square root of the number of protons. From the data interpolation it is possible to retrieve the number of protons that guarantees a maximum precision in range retrieval as illustrated on the graph. For this case, 1.4×10^8 protons results in a precision of 4 mm.

4.2.3. Range control. The detection profiles at different positions of the target are shown in figure 14 for 100 MeV (left) and 160 MeV (right) pencil beams. The number of incident protons was of the order of magnitude of 10^{11}. For this high level of dose, profiles are distinguishable from one another by visual inspection.

The exact shift with respect to the 0 mm profiles is plotted in figure 15(*a*). The *x*-axis represents the retrieved shift, while the *y*-axis represents the expected shift, i.e. the position of the target with respect to the central position. At 100 MeV, the data trend follows the expected behavior, illustrated with a dashed line, while at 160 MeV the retrieved shift tends to be lower than expected. Results of figure 15(*a*) are relative to high statistics profiles; the mean absolute range error for different levels of dose is shown in figure 15(*b*).

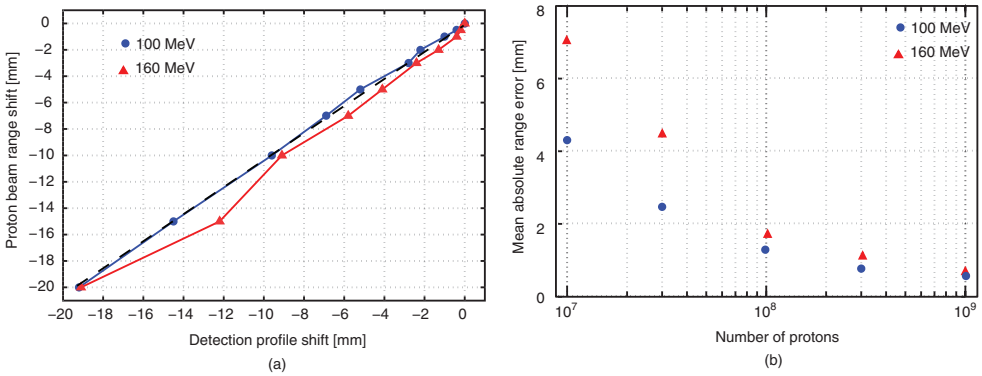

Figure 15. (*a*) Exact shift of the proton beam range as a function of the shift of the fit of the acquired detection profile for pencil beams of 100 (blue line) and 160 MeV (red line). The dashed line indicates the ideal trend. (*b*) Mean asbolute range error as a function of the number of incident protons for pencil beams of 100 (blue circles) and 160 MeV (red triangles)

4.2.4. Profiles at different beam energies. Profiles measured with the camera centered at the expected range depth for 100 MeV, 160 MeV and 230 MeV pencil beams are shown in figure 16. The 10 s acquisitions were normalized to the number of protons delivered that is equal to 7.07×10^{10} at 100 MeV, 1.14×10^{11} at 160 MeV and 2.86×10^{11} at 230 MeV. In the left column the smoothed and normalized acquisitions acquired in the open and closed collimator configurations are shown. On the same graphs, the simulations are depicted with light colors. Measurements and simulations show very nice agreement at 100 MeV in both collimator configurations. Simulations and measurements are in worse agreement at 160 MeV and 230 MeV, especially if we consider the acquisition with the collimator open, that includes both the correlated contribution due to prompt gammas and the uncorrelated contribution. In the present comparison we can observe that the simulation overestimates the prompt gamma signal, while the numbers of neutrons and uncorrelated events are quite similar to these obtained from measurement.

The results of the analysis of profiles after the subtraction of the uncorrelated contribution are presented in the right column of figure 16. The best match between measurements and simulations was obtained by scaling the simulation for a factor 0.91, 0.76 and 0.74. After rescaling, simulations and profiles show relatively good agreement, especially in the fall-off region and at low energy.

The range precision for different numbers of protons is presented in figure 17. The number of protons to reach a precision of $2\sigma = 4$ mm increases with energy and it is 0.5×10^8, 1.4×10^8 and 3.4×10^8 for the three energies, respectively. That means that a higher dose is needed to obtain the same precision at higher beam energies. In the right column the number of events detected by the camera is plotted versus the number of protons.

4.2.5. Profiles in different energy windows. Profiles acquired by applying different selection windows are shown in figure 18. About 10^{11} protons were delivered during each acquisition. Red lines refer to the acquisitions with the collimator open and the blue lines to the acquisitions with the collimator closed and a vertical line indicates the beam range within the target. From the graphs, it is clear that a good profile was acquired in the 1–2, 2–3, 3–4, 4–5 and 5–6 MeV energy ranges, while at higher energies the profiles start to degrade, in

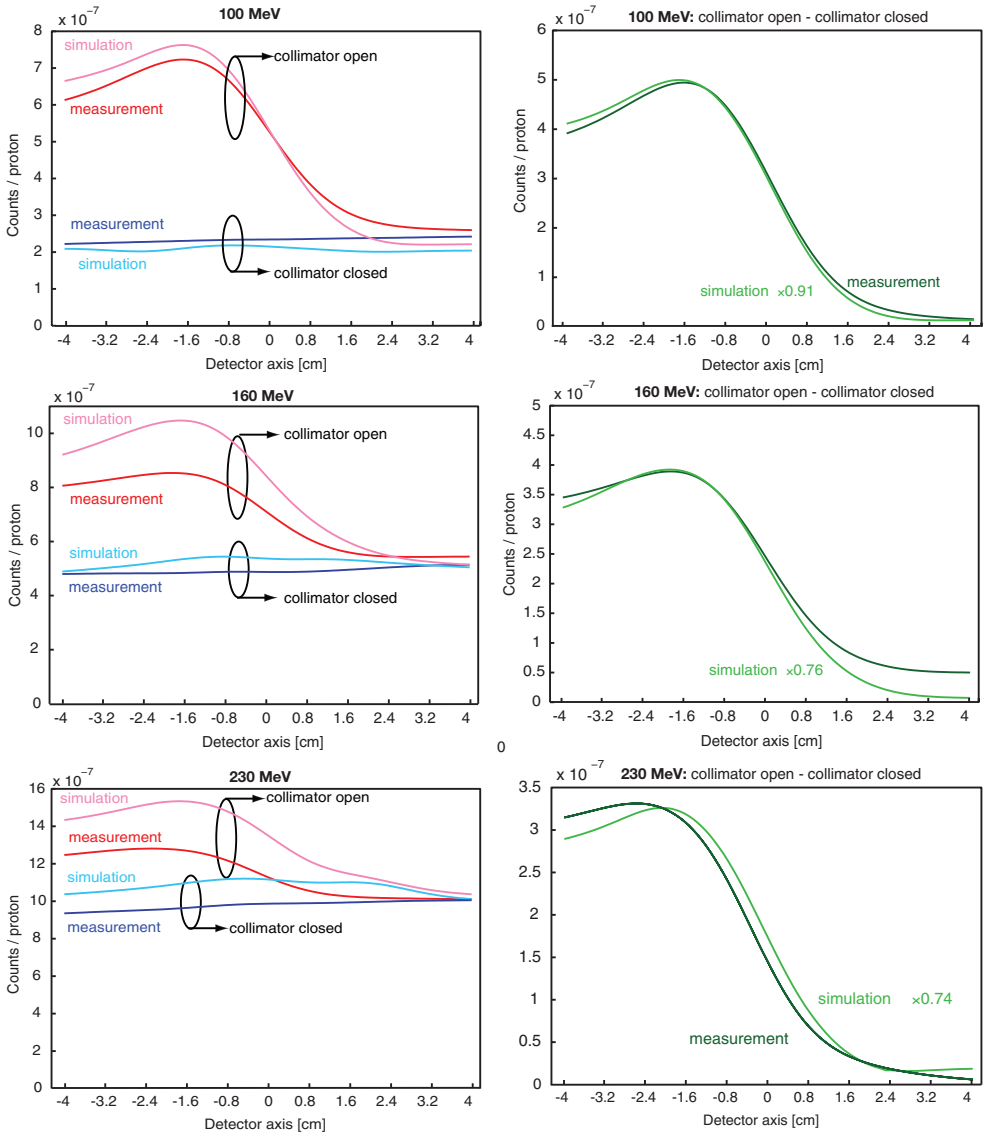

Figure 16. Detection profiles measured with the camera centered at the expected range depth of 100 MeV, 160 MeV and 230 MeV pencil beams. On the left the profiles acquired with the collimator open and closed and the respective simulation are shown. On the right the profiles acquired with the collimator open are subtracted from the uncorrelated contribution. The simulations are scaled to fit the acquisitions

such a way that the shape is no more pertinent and the precision could not be calculated. The number of protons to achieve a 4 mm precision was quantified for the pertinent energy windows and is equal to 8×10^8, 6.5×10^8, 3.2×10^8, 4.7×10^8 and 8.5×10^8 for 1–2, 2–3, 3–4, 4–5 and 5–6 MeV, respectively. The 3–4 MeV and 4–5 MeV windows give the best contribution but a nice value was found also in the 2–3 MeV range, suggesting that the selection window could be extended to improve the statistics. This confirmed that the

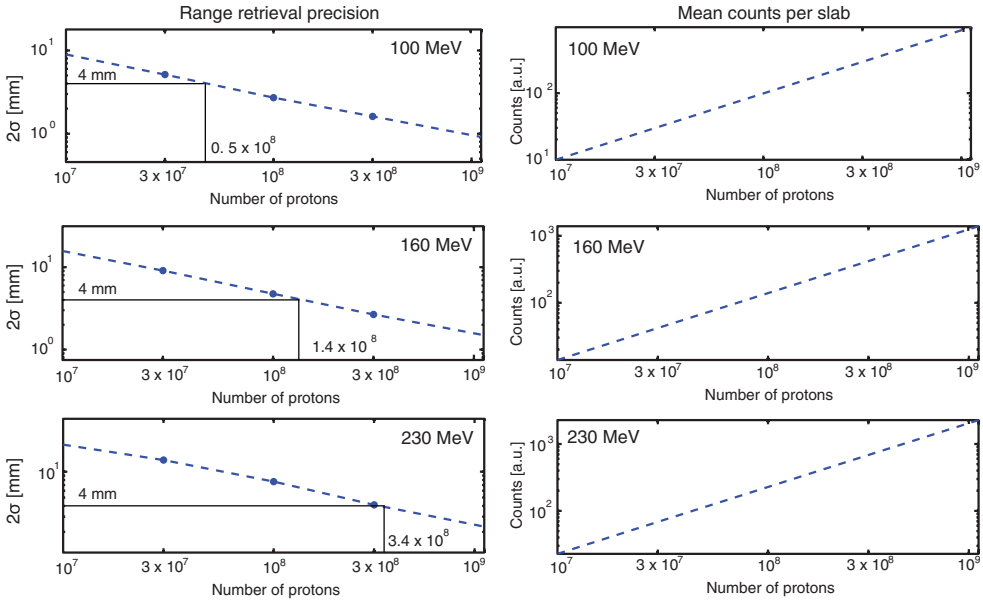

Figure 17. Range shift precision with respect to the number of protons and mean number of counted events for 100 MeV, 160 MeV and 230 MeV. Data originate from measured profiles.

energy window from 1 MeV to 6 MeV resulted in better correlated profiles compared to higher energies.

4.2.6. Measurement of the entrance point. In figure 19, acquired profiles of the entrance point are compared to the fall-off profiles for 100 MeV, 160 MeV and 230 MeV beams and 7.36×10^{10}, 1.16×10^{11} and 2.66×10^{11} protons. The minimum number of protons for a precision inferior to 4 mm is 1.4×10^8, 3.5×10^8 and 3.7×10^8, respectively. These values are higher compared to the ones obtained for the fall-off region (0.5×10^8, 1.4×10^8 and 3.4×10^8). One should note that the design of the camera was optimized for the measurement of the fall-off. Prompt gammas are adequately suited to the measure of the Bragg peak position in the patient as their high energies give them the possibility to exit from the patient, even from deep-seated tumours. This is not really an advantage for the measurement of the entrance point and other modalities would also deserve consideration, such as the use of external detectors that track the location of the surface of the patient in the treatment room.

4.2.7. Profiles at different beam currents. Profiles obtained at different beam currents are shown in in figure 20(*a*). The number of delivered protons is reported in table 2 for each value of beam current. The plots represent raw data before smoothing and normalization for the number of protons delivered; on the *y*-axis the number of acquired events in the 3–6 MeV energy range during the 10 s acquisition is visible. The maximum count rate during each acquisition is plotted with respect to the beam current in figure 20(*b*). In a perfect system with 100% efficiency this curve would have a linear trend, because we expect the event rate to increase with the beam current. Actually, we notice a saturation of the detected rate with the current, meaning that the dead-time affects the efficiency of the camera. Even if the maximum rate scored

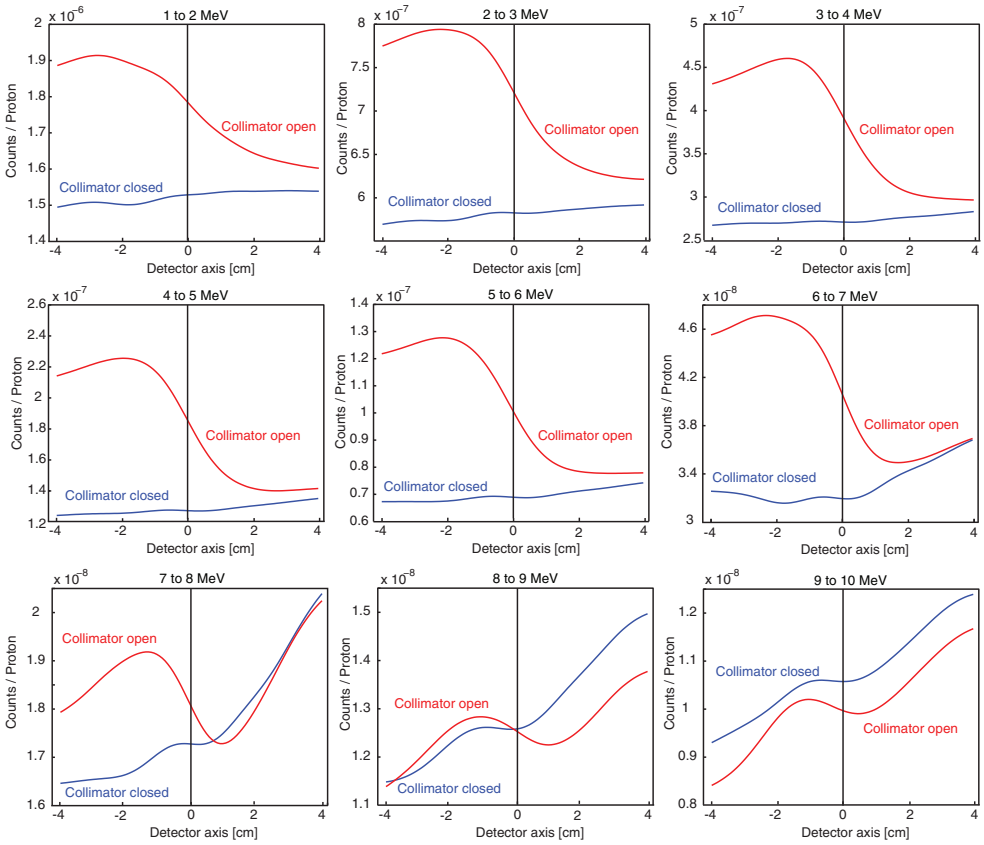

Figure 18. Detection profiles measured at 160 MeV with different energy windows. The red line is relative to the acquisition with the collimator open and the blue one to the acquisition with the collimator closed. The proton range is indicated with a vertical bar.

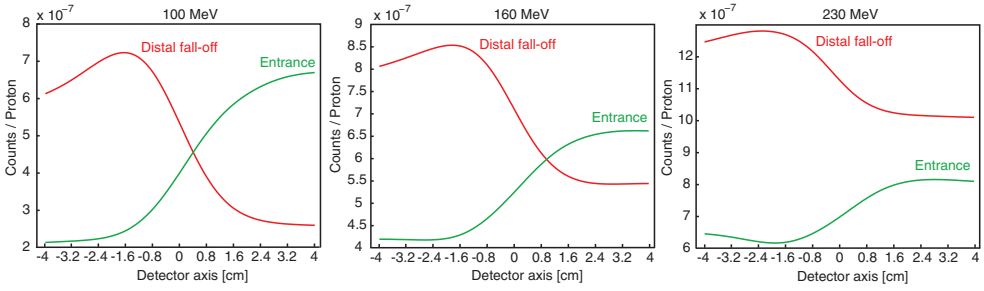

Figure 19. Detected profiles centered on the entrance point in the target. A comparison with the distal fall-off acquisition is shown in red. Proton range and target entrance are located at detector axis 0 cm, respectively.

is 350 kHz, we have to take into consideration the fact that the energy spectrum is continuous and the events in the 3–6 MeV range represents only 4.4% of events of the whole spectrum. According to spectra acquisition, we expect a rate of 8 MHz with a beam current of 28.8 nA.

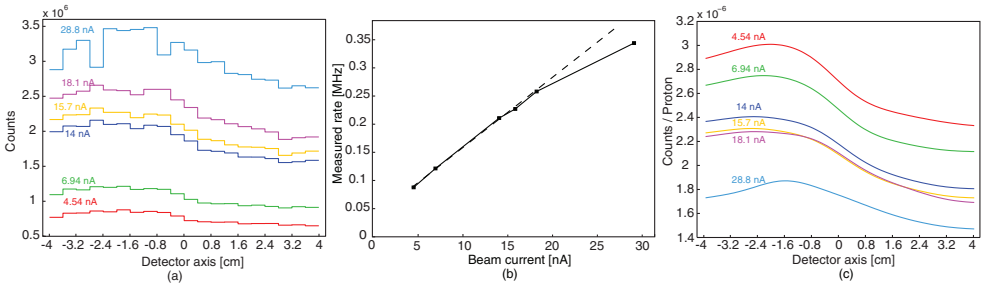

Figure 20. (*a*) Detection profiles measured at 230 MeV at different beam currents (raw data before normalization to the number of protons). (*b*) Measured rate at different beam currents in the 3–6 MeV energy window. Data have a linear trend (dashed line) until 18 nA. (*c*) Detection profiles at different beam currents after smoothing and normalization to the number of delivered protons.

Table 2. Beam currents for the experiments of count rate capability. For each value of current the number of delivered protons during the acquisition and the number of protons to reach a 4 mm precision are reported.

Beam current (nA)	Protons delivered	Protons for 4 mm precision
4.54	2.84×10^{11}	1.4×10^{8}
6.94	4.34×10^{11}	1.4×10^{8}
14.00	8.72×10^{11}	1.9×10^{8}
15.70	9.82×10^{11}	2.0×10^{8}
18.10	1.13×10^{12}	2.1×10^{8}
28.80	1.80×10^{12}	2.8×10^{8}

This rate is mainly due to the very low energy events that have no impact on the profile acquisition but worsen the pile-up effect, degrading the counting efficiency.

The third graph of figure 20 is the plot of the profiles after normalization to the number of protons and smoothing. The profiles are not coincident because the efficiency of the counting system is lower at higher currents, hence higher rates. That results in a lower number of detected events per proton. The camera is able to acquire profiles even at currents higher than the clinical values, but dead-time correction would be needed. A model for dead-time correction is still under investigation.

The reduced efficiency results in worse performances in shift retrieval: a higher number of protons is needed to achieve the same error of 4 mm: the exact values are listed in table 2.

5. Conclusion

In this work we presented the first gamma camera suitable for proton beam range measurement at clinical beam current. A totally dedicated design was chosen to optimize several parameters needed for prompt gamma imaging using a slit-collimator. The dimensions and geometry of the LYSO scintillator were chosen to reach high statistics (with a 3 cm thick crystal) and high count rates (with a pixelated scintillator). Silicon photomultipliers were chosen as visible light photo-detectors for their small size (suitable for 1 : 1 coupling with the pixelated scintillator), high speed, low noise and good quantum efficiency. The front-end electronics were designed both to perform energy calibration at low rates and fast counting of events in the energy range of interest. A compact and portable camera was designed to be compatible

with a real treatment room. To benchmark several aspects of the design, a small prototype, limited to 2 channels was constructed and tested in laboratory with the use of low-activity and low energy radiation sources. The results confirmed the possibility to extend the design to a full-size prototype. Up to now, we have mounted only half of the final prototype detectors (20 channels) and tested the system with proton beams of 100 MeV, 160 MeV and 230 MeV at clinical beam currents of several nA. The measurements demonstrate the ability of the camera to detect millimetric shifts of the target for high levels of dose. Acquired profiles and simulations were compared and show good agreement, especially at 100 MeV and we achieved precision of 4 mm (2σ) for 0.5×10^8, 1.4×10^8 and 3.4×10^8 protons at 100 MeV, 160 MeV and 230 MeV, respectively. Measurements also confirmed that, at the 3–6 MeV selection window, the system has good precision in range retrieval and that the precision is better in detecting the fall-off than the entrance point. The capability of the camera to work at high count rates was verified by acquiring profiles in very challenging conditions with currents of tens of nA at 230 MeV. Although a lower efficiency was observed, the shape of the profile and the precision are still satisfactory. We are now working on the completion of the camera with the second half, in order to reach the requested sensitivity. Different configurations and compositions of the target will be tested as well. A dead-time model is under investigation to correct high count rate profiles.

Acknowledgments

This work received funding from the European Union Seventh Framework Program (FP7/2007-2013) under grant agreement nos 241851 (ENVISION) and 264552 (ENTERVISION).

We would like to thank Ben Reynders, Eric Demoitié and Riccardo Saitta from IBA for their precious contributions to the preparation and realization of the measurements and Brian Hutton from UCL for the revision of the manuscript.

References

Anger H O 1967 Radioisotope cameras *Instrumentation in Nuclear Medicine* vol 1 ed Hine G J (New York: Academic) pp 485–552

Bauer J *et al* 2013 Implementation and initial clinical experience of offline PET/CT-based verification of scanned carbon ion treatment *Radiother. Oncol.* **107** 218–26

Bom V, Joulaeizadeh L and Beekman F 2011 Real-time prompt gamma monitoring in spot-scanning proton therapy using imaging through a knife-edge shaped slit *Phys. Med. Biol.* **57** 297–308

Ekström L P and Fireston R B 1999 *WWW Table of Radioactive Isotopes (version 2.1)* (Berkeley, CA: Lawrence Berkeley National Laboratory)

Enghardt W, Crespo P, Fiedler F, Hinz R, Parodi K, Pawelke J and Ponisch F 2004 Charged hadron tumour therapy monitoring by means of PET *Nucl. Instrum. Methods Phys. Res.* A **525** 284–8

Gottschalk B *et al* 2011 Water equivalent path length measurement in proton radiotherapy using time resolved diode dosimetry *Med. Phys.* **38** 2282–8

Grodzicka M *et al* 2011 Effective dead time of APD cells of SIPM *IEEE Nuclear Science Symp. Conf. Record (ESP, Valencia, 23–29 October 2011)* pp 553–62

Helmbrecht S, Enghardt W, Parodi K, Didinger B, Debus J, Kunath D, Priegnitz M and Fiedler F 2013 Analysis of metabolic washout of positron emitters produced during carbon ion head and neck radiotherapy *Med. Phys.* **40** 091918

Hirano Y, Kniouchi S, Ikoma Y, Yoshida E, Wakizaka H, Ito H and Yamaya T 2013 Compartmental analysis of washout effect in rat brain: in-beam OpenPET measurement using a ^{11}C beam *Phys. Med. Biol.* **58** 8281

Kim C H, Min C H, Seo K S and Kim J W 2007 Simulation studies on the correlation of distal dose falloff of a 70 MeV proton beam with a prompt gamma distribution *J. Korean Phys. Soc.* **50** 1510–3

Knopf A *et al* 2009 Systematic analysis of biological and physical limitations of proton beam range verification with offline PET/CT scans *Phys. Med. Biol.* **54** 4477–95
Knopf A C and Lomax A 2013 *In vivo* proton range verification: a review *Phys. Med. Biol.* **58** R131–60
Kormoll T *et al* 2011 A Compton imager for *in-vivo* dosimetry of proton beams—a design study *Nucl. Instrum. Methods Phys. Res.* A 626–7
Kozlovsky B, Murphy R J and Ramaty R 2002 Nuclear deexcitation gamma-ray lines from accelerated particle interactions *Astrophys. J. Suppl. Ser.* **141** 523–41
Kurosawa S *et al* 2012 Prompt gamma detection for range verification in proton therapy *Curr. Appl. Phys.* **12** 364–8
Metzler S D and Accorsi R 2005 Resolution-versus sensitivity-effective diameter in pinhole collimation: experimental verification *Phys. Med. Biol.* **50** 5005–17
Min C H, Kim C H, Youn M Y and Kim J W 2006 Prompt gamma measurements for locating the dose falloff region in the proton therapy *Appl. Phys. Lett.* **89** 183517
Min C H *et al* 2012 Development of array-type prompt gamma measurement system for *in vivo* range verification in proton therapy *Med. Phys.* **39** 2100–7
Mizuno H *et al* 2003 Washout measurement of radioisotope implanted by radioactive beams in the rabbit *Phys. Med. Biol.* **48** 2269
Nishio T, Miyatake A, Ogino T, Nakagawa K, Saijo N and Esumi H 2010 The development and clinical use of a beam ON-LINE PET system mounted on a rotating gantry port in proton therapy *Int. J. Radiat. Oncol. Biol. Phys.* **76** 277–86
Paganetti H 2012 Range uncertainties in proton therapy and the role of Monte Carlo simulations *Phys. Med. Biol.* **57** R99–117
Parodi K *et al* 2007 Patient study of *in vivo* verification of beam delivery and range, using positron emission tomography and computed tomography imaging after proton therapy *Int. J. Radiat. Oncol. Biol. Phys.* **68** 920–34
Parodi K, Bortfeld T, Enghardt W, Fiedler F, Knopf A, Paganetti H, Pawelke J, Shkirin G and Shih H 2008 PET imaging for treatment verification of ion therapy: implementation and experience at GSI Darmstadt and MGH Boston *Nucl. Instrum. Methods Phys. Res.* A **586** 133–42
Perali I *et al* 2012 Prompt gamma imaging with a slit camera for real-time range control in proton therapy: experimental validation up to 230 MeV with HICAM and development of a new prototype *IEEE Nuclear Science Symp. Conf. Record (Anaheim, CA, USA, 29 October–03 November 2012)* pp 3883–6
Peterson S W, Robertson D and Polf J 2010 Optimizing a three-stage Compton camera for measuring prompt gamma rays emitted during proton radiotherapy *Phys. Med. Biol.* **55** 6841–56
Prieels D, Smeets J, Stichelbaut F, Benilov A, Dehaes J C, Dubus A and Roellinghoff F 2011 Towards a practical solution for real-time measurement of the proton beam range in patients *50th Meeting of the Particle Therapy Co-Operative Group (Philadelphia, PA, 8—14 May 2011)*
Richard M-H *et al* 2011 Design guidelines for a double scattering Compton camera for prompt-gamma imaging during ion beam therapy: a Monte Carlo simulation study *IEEE Trans. Nucl. Sci.* **58** 87–94
Schneider U and Pedroni E 1995 Proton radiography as a tool for quality control *Med. Phys.* **22** 353–63
Schneider U *et al* 2012 Spatial resolution of proton tomography: methods, initial phase space and object thickness *Z. Med. Phys.* **22** 100–8
Seo H *et al* 2007 Monte Carlo study of a double-scattering compton camera with GEANT4 *Nucl. Instrum. Methods Phys. Res. A* **580** 314–7 *(Proc. 10th Int. Symp. Radiation Physics)*
Smeets J *et al* 2012 Prompt gamma imaging with a slit camera for real-time range control in proton therapy *Phys. Med. Biol.* **57** 3371–405
Stichelbaut F and Jongen Y 2003 Verification of the proton beams position in the patient by the detection of prompt gamma-rays emission *39th Meeting of the Particle Therapy Co-Operative Group (San Francisco, CA, October 2003)*
Testa M *et al* 2010 Real-time monitoring of the Bragg-peak position in ion therapy by means of single photon detection *Radiat. Environ. Biophys.* **49** 337–43
Tomitani T *et al* 2003 Wahsout studies of ^{11}C in rabbit thigh muscle implanted by secondary beams of HIMAC *Phys. Med. Biol.* **48** 875